Journal of Materials Chemistry A

ROYAL SOCIETY OF CHEMISTRY

PAPER

View Article Online
View Journal

Check for updates

Cite this: DOI: 10.1039/d5ta03873a

Deciphering the functions of rubidium in structural stability and ionic conductivity of KAg_4I_5

Haitao Wang, Te Kang, Long Yang * and Yanzhong Pei *

Received 14th May 2025
Accepted 8th August 2025

DOI: 10.1039/d5ta03873a

rsc.li/materials-a

Solid electrolytes, a key component of all solid-state ion batteries, have gained considerable attention for their high safety and chemical stability. Two key metrics for solid electrolytes are ionic conductivity and structural stability. Herein, we found that both metrics can be improved by the collaborative effects of rubidium substitution in KAg_4I_5 solid electrolytes. $K_{0.8}Rb_{0.2}Ag_4I_5$ was obtained through a melting method, achieving an ionic conductivity of 0.15 S cm^{-1} and a low activation energy of 19 meV, because K^+ (1.38 Å) was partially replaced by Rb^+ with a larger ionic radius of 1.52 Å, resulting in a larger and wider silver ion migration channel. The three-dimensional silver ion diffusion pathway in KAg_4I_5 was determined by the maximum entropy method analysis experimentally. Rb^+ doping changes the local chemical environment of KAg_4I_5, which increases the energy barrier required for phase transition and decomposition, enhancing the structural stability. The resulting performance suggests that the designed electrolyte $K_{0.8}Rb_{0.2}Ag_4I_5$ has a promising application potential for silver-ion solid batteries.

1. Introduction

Solid-state electrolytes (SSEs) have emerged as a transformative class of materials characterized by high ionic conductivity, enabling efficient ion transport through well-defined migration pathways. A pivotal breakthrough occurred in 1961 when Ag_3SI and Ag_3SBr were discovered, exhibiting an unprecedented ionic conductivity of $\sim10^{-2}$ S cm^{-1} at room temperature, far surpassing the previously limiting threshold of $\sim10^{-6}$ S cm^{-1}.[1] This discovery unlocked new possibilities for SSE applications and spurred extensive research into diverse ion-conducting materials, including Ag^+-based halides, oxygen-ion conductors, and Na^+-conducting ceramics.[2–5] SSEs offer unique advantages over conventional liquid electrolytes, including broader operational temperature ranges, enhanced safety, and negligible electronic conductivity. While most liquid electrolytes exhibit higher ionic conductivity, a few solid-state superionic conductors can achieve comparable performance.[6–8] These properties have established SSEs as key foundations for a range of advanced technologies, such as high-energy-density solid-state batteries, electrochromic and memory devices, and precision ionic sensors.[9–12]

Ionic conductivity is one of the most important characteristics of SSEs. However, it remains challenging to prepare high-performance solid electrolytes with high ionic conductivity as well as exhibit high chemical and thermal stabilities.[13–15] Owing to the superionic conductivity of >1 S cm^{-1}, superior to the existing lithium-based or sodium-based solid electrolytes and comparable to the best liquid electrolyte, the α-AgI phase has aroused extensive interest from scientists and technologists as a potential solid-state electrolyte candidate.[16–18] The exceptionally high ionic conductivity of α-AgI ($\sim$1 S cm^{-1}) is attributed to the "liquid-like" diffusion of Ag^+, which arises from its highly disordered structural arrangement.[19–21] The anion lattice provides more sites than the number of Ag^+, and these sites are occupied in a largely random manner. This structural disordering enables efficient ionic migration within the partially occupied Ag sublattice.[16,22,23] However, a dramatic drop of about 4 orders of magnitude occurs in the ionic conductivity due to the phase transition into poorly conductive β-AgI when below 420 K, thereby severely limiting its practical application.[24,25] Therefore, many efforts have been devoted to stabilize the α-AgI phase at room temperature through the following strategies.

The α-AgI phase can be stabilized within a glass matrix at room temperature exhibiting a high ionic conductivity of $\sim$0.1 S cm^{-1}.[17,26,27] For example, α-AgI was successfully stabilized in AgI–Ag_2O–B_2O_3 glass ceramic at room temperature through a twin-roller rapid quenching technique.[28] Meanwhile, the ionic conductivity of AgI-based phosphate glasses can be improved following an appropriate crystallization process.[29] Besides, by reducing the size of AgI into nanoscale particles, the α- to β-/γ-AgI phase transition temperature can be decreased to room temperature.[18,30] Furthermore, the high-temperature phase (α-AgI) can be stabilized below 420 K by substituting the cations or anions in the AgI compound.[16] These strategies are promising to be implemented in synthesizing ternary phases derived from AgI to achieve high ionic conductivity at lower operational temperatures.

Interdisciplinary Materials Research Center, School of Materials Science and Engineering, Tongji University, Shanghai 201804, China. E-mail: long_yang@tongji.edu.cn; yanzhong@tongji.edu.cn

In the case of the AgI–KI system, two compounds, K_2AgI_3 and KAg_4I_5 were identified.[31] The former is stable up to ∼400 K but exhibits poor conductivity. KAg_4I_5 was found to be stable over the temperature range from 311 K to its congruent melting point of 526 K and possesses a high value of ionic conductivity. In this work, stabilization was achieved for KAg_4I_5 at room temperature through Rb^+ doping, significantly enhancing its stability under ambient conditions. The larger ionic radius of Rb^+ compared to K^+ effectively broadened the ionic conducting channels, leading to an improvement in ionic conductivity. The migration pathways of silver ions in KAg_4I_5 are revealed by the electron density distribution obtained through maximum entropy method (MEM) reconstruction.

2. Experimental section

The starting materials, AgI powder (Sigma-Aldrich, 99.99%), KI powder (Sigma-Aldrich, 99.99%) and RbI powder (Sigma-Aldrich, 99.99%), were used as received. Stoichiometric amounts of the elements were loaded into silica ampoules and flame-sealed under vacuum. The ampoules were placed in a tube furnace and heated to 973 K over 6 h and annealed at 440 K for 36 h before cooling to room temperature. The resulting products are silver ingots, which were subsequently ground with a mortar and pestle before further use.

The structural characterization of the synthesized electrolyte was performed using various analytical techniques. The powder X-ray diffraction (XRD) measurements of $K_{1-x}Rb_xAg_4I_5$ (x = 0–0.3) used for Rietveld refinement were performed using a Japan Rigaku SmartLab system with Cu Kα radiation (λ = 0.154 nm). The 2θ angle range was set from 5° to 90°, with a step size of 0.02° and an exposure time of 0.60 s per step. The Rietveld refinement for fitting the crystalline structure was performed using GSAS-II software.[32] The cubic structure KAg_4I_5 has a space group of $P4_132$.[33] The refinable parameters including lattice constants, atomic positions allowed by the space group, and the isotropic atomic displacement parameters (U_{iso}) of each atom, were set to be the same for atoms occupying the same crystallographic symmetry sites. R_{wp} is the goodness-of-fit parameter in Rietveld refinement. The electron density distributions were analyzed from the observed structure factor by the MEM method, based on the Dysnomia program.[34,35] The crystal structures and the electron density distribution iso-surfaces were visualized using VESTA.[36]

For X-ray photoelectron spectroscopy (XPS) spectra, a Thermo Scientific K-Alpha$^+$ spectrometer system equipped with a monochromatic Al K$_\alpha$ source was employed. The microstructures and elemental distribution were confirmed using a scanning electron microscope (SEM, Phenom Pro) equipped with an energy dispersive spectrometer (EDS).

For the electrochemical measurements, 300 mg of solid electrolyte was weighed and pressed into a pellet in a battery mold under a pressure of 0.2 t. The molded battery was then tested using alternating current (AC) impedance spectroscopy to measure the impedance characteristics of the sample. The ionic conductivity of the electrolyte was then calculated based on the obtained impedance data. DC polarizations were conducted in the voltage range from 0.1 to 0.5 V.

3. Results and discussion

The XRD data of $K_{1-x}Rb_xAg_4I_5$ (x = 0–0.3) in Fig. 1a are well indexed to the standard pattern of KAg_4I_5 (PDF no. 29-1034), indicating that the synthesized samples are in a single phase. The enlarged XRD pattern over the 2θ range of 26–27° clearly reveals that the (311) diffraction peak gradually shifts towards lower angles with more Rb content. The experimental XRD patterns and refinement results of $K_{1-x}Rb_xAg_4I_5$ (x = 0–0.3) samples are shown in Fig. 1b–e. More detailed refinement results are listed in Tables S1–S4. The lattice parameters of $K_{1-x}Rb_xAg_4I_5$ (x = 0–0.3) were determined by Rietveld refinement results, yielding parameter a values of 11.1370, 11.1535, 11.1637, and 11.1763 Å for x = 0, 0.1, 0.2, and 0.3, respectively. When the larger ionic radius of Rb^+ (1.52 Å) is introduced into the site occupied by K^+ (1.38 Å), the lattice would expand, resulting in an increase in the lattice constant and

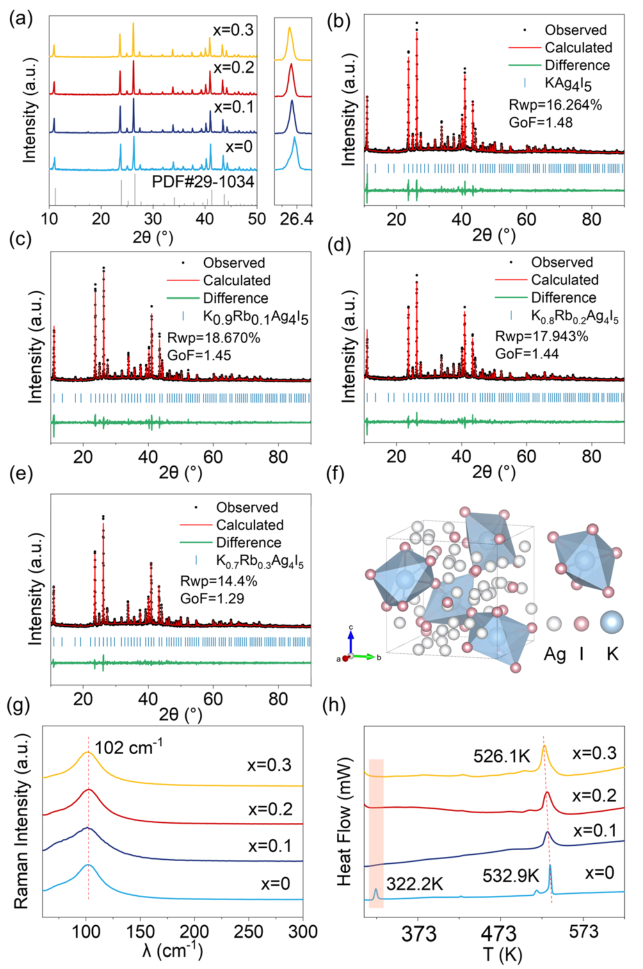

Fig. 1 (a–e) XRD patterns and the corresponding Rietveld refinement results for $K_{1-x}Rb_xAg_4I_5$ (x = 0–0.3). (f) Crystal structure of KAg_4I_5. (g) Room-temperature Raman spectrum of $K_{1-x}Rb_xAg_4I_5$ (x = 0–0.3). (h) Temperature dependent heat flow for $K_{1-x}Rb_xAg_4I_5$ (x = 0–0.3).

a corresponding shift of the diffraction peak to lower angles. These results demonstrate the successful incorporation of Rb^+ into the lattice site, thus validating the feasibility of the Rb^+ doping strategy.

Based on the XRD refinements, Fig. 1f shows the crystal structure of KAg_4I_5, which adopts a complicated cubic structure at room temperature. In this arrangement, K^+ ions occupy a distorted octahedral coordination environment, while Ag^+ ions are predominantly distributed over two distinct sites, both of which are tetrahedrally coordinated with I^-. The unit cell contains four formula units, and the structure is highly distorted since the 16 Ag^+ ions are randomly distributed over 48 atomic sites.

To further investigate the structural effects of Rb^+ doping in KAg_4I_5, Raman spectroscopy was conducted, and the results are shown in Fig. 1g. The characteristic Raman peak at 102 cm^{-1} is attributed to the lattice vibrational modes involving Ag^+ and I^- ions. Notably, no significant shift in the Raman peak position was observed after doping, indicating that the doping process did not induce substantial structural changes, and the primary structural framework and vibrational modes of the material were retained.

As illustrated in Fig. 1h, differential scanning calorimetry (DSC) measurements were performed on KAg_4I_5 and its rubidium-doped variants ($K_{1-x}Rb_xAg_4I_5$ ($x = 0$–0.3)) to elucidate the effects of Rb^+ doping on thermal stability and phase transitions. For pristine KAg_4I_5, no significant mass loss was observed in Thermogravimetric Analysis (TGA) (Fig. S2), while DSC revealed endothermic peaks at 322.2 K, 516.7 K and 532.9 K, which correspond to distinct phase transitions or decompositions. Notably, with increasing Rb^+ doping concentration, the endothermic peak at a lower temperature of 322.2 K was gradually suppressed and eliminated eventually. This result indicates that the introduction of Rb^+ inhibits the disproportionation of KAg_4I_5 into K_2AgI_3 and AgI, maintaining a stable phase from room temperature up to 493 K. The underlying mechanism is associated with structural modifications, which stabilize the low-temperature phase by increasing the energy barrier for the phase transition, thereby removing the corresponding peak from the DSC curves. Additionally, a shift of the high-temperature endothermic peak from 532.9 K to 526.1 K was observed upon Rb doping, suggesting that Rb^+ incorporation leads to a reduction in the phase transition temperature. To further investigate the enhanced structural stability induced by Rb doping, we performed a comparative analysis of the phase transition energetics through differential scanning calorimetry. The measured transition enthalpy (ΔH) shows a significant 16.4% increase from 15.9 J g^{-1} for pristine KAg_4I_5 to 18.5 J g^{-1} for $K_{0.8}Rb_{0.2}Ag_4I_5$ (Fig. S3), providing direct thermodynamic evidence that the doped material requires substantially more energy to undergo phase transformation. This elevated energy requirement for phase transformation indicates a substantial increase in the activation barrier for structural rearrangement, directly quantifying the stabilization effect of Rb incorporation.

X-ray photoelectron spectroscopy (XPS) was employed to investigate the chemical composition and states of the as-prepared materials. As shown in Fig. 2a–e, four peaks in XPS spectra correspond to Rb 3d, K 2p, Ag 3d, and I 3d, respectively. Compared to pristine KAg_4I_5, the K 2p peak in the doped sample exhibited a slight shift towards higher energy, suggesting a change in the chemical environment of K^+ due to the charge density redistribution by Rb^+ incorporation. In the Rb-doped sample, the Rb 3d peak was observed at approximately 111.6 eV and 110.1 eV, corresponding to the spin–orbit split of Rb $3d_{5/2}$ and Rb $3d_{3/2}$, indicating successful incorporation of Rb^+ into the lattice. The peak at 110.17 eV was attributed to Rb–I bonding, while a shoulder peak at 111.64 eV was potentially associated with a loss feature due to strong interactions with free Ag^+ ions within the lattice. The I 3d peaks also showed a subtle energy shift, reflecting minor changes in the electronic environment of the iodine atoms. The Ag 3d spectrum exhibited spin–orbit split peaks at approximately 368.45 eV (Ag $3d_{5/2}$) and 374.35 eV (Ag $3d_{3/2}$), with a binding energy separation of 6.0 eV, which is the characteristic of metallic Ag and Ag^+ ions. According to the crystal structure of KAg_4I_5, the presence of both ordered and disordered Ag–Ag bonds was observed. A slight increase in the binding energy of the Ag 3d peak in the doped sample further indicated that the chemical environment of silver was affected by Rb^+ doping. In conclusion, the incorporation of Rb^+ resulted in a redistribution of electron density within the crystal structure, potentially influencing the electronic, thermal, and electrochemical properties of the material.

Electrochemical impedance spectroscopy (EIS) was carried out to evaluate both the ionic conductivities and the activation energies for Ag^+ transport in all electrolytes. The electrolyte pellets used for testing were obtained by cold-pressing the powder in a mold. Fig. 3e depicts the impedance complex plane of $K_{1-x}Rb_xAg_4I_5$ ($x = 0$–0.3) electrolytes at room temperature. The corresponding Nyquist plots of EIS for each electrolyte, measured at different temperatures, are depicted in Fig. 3a–d. All the samples show no high frequency arcs because the resistance of grain boundary is too low to be detected. The ionic conductivity values were obtained from the intercepts of these Nyquist plots on the real Z' axis. The temperature dependence of the ionic conductivity of these samples is shown in Fig. 3f, and the activation energy (E_a) was calculated from the slope of the temperature dependence. The conductivity *versus* temperature is fitted well using the Arrhenius equation:

$$\sigma_i = \frac{A}{T}\exp(-E_a/k_BT) \tag{1}$$

where T is the absolute temperature, A is the pre-exponential factor, E_a is the activation energy for conduction, and k_B is the Boltzmann constant.

The ionic conductivity of KAg_4I_5 in Fig. 3f appears to deviate from the Arrhenius behavior. The non-Arrhenius behavior is attributed to a reversible phase transition near 322 K ($2KAg_4I_5 = K_2AgI_3 + 7AgI$), as evidenced by the distinct endothermic peak in DSC results (Fig. 1h). Notably, the phase transition is suppressed at higher Rb^+ doping levels, as indicated by the disappearance of the peak at 322 K, which correlates with better linear fitting of the conductivity data. The composition dependence of the activation energy and conductivity is plotted in Fig. 3g. The ionic conductivity of KAg_4I_5 was found to be 0.04 S

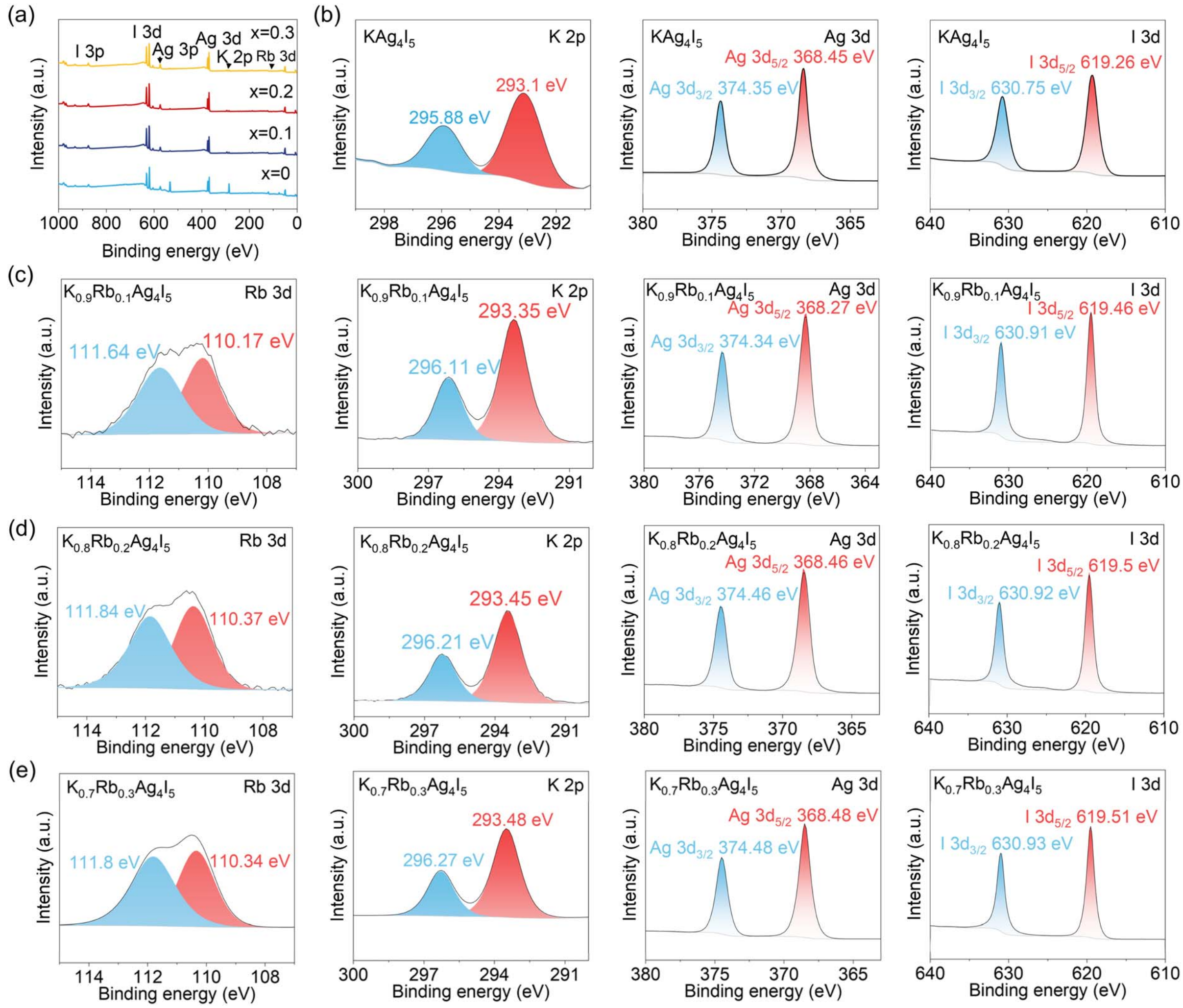

Fig. 2 X-ray photoelectron spectroscopy (XPS) spectra of $K_{1-x}Rb_xAg_4I_5$. (a) Survey spectra. (b–e) High-resolution spectra of Rb 3d, K 2p, Ag 3d and I 3d electrons for $K_{1-x}Rb_xAg_4I_5$ (x = 0–0.3) respectively.

cm^{-1} at room temperature, exhibiting an increase to 0.15 S cm^{-1} in the case of $K_{0.8}Rb_{0.2}Ag_4I_5$ electrolyte. It can be attributed to the lattice expansion, facilitating the Ag^+ diffusion path and considerably improving the ionic conductivity of the solid electrolyte. However, with varying Rb dopant amounts, it linearly decreased to 0.13 S cm^{-1} for the $K_{0.7}Rb_{0.3}Ag_4I_5$ electrolyte. This decrease may be attributed to the situation that excessive Rb doping may distort the lattice structure, ultimately degrading the effective ion migration channels and lowering the overall ionic conductivity of KAg_4I_5. The activation energy change exhibited an overall opposite trend to ionic conductivity. The activation energies (E_a) show 125, 23, 19 and 5 meV for $K_{1-x}Rb_xAg_4I_5$ (x = 0–0.3) electrolytes, respectively. In general, lower E_a means faster ion migration, and it is promising to implement the electrolytes in a wider temperature range.

The relationship between the structure and activation energies in the diffusion process is important to understand the underlying operation mechanism. To address this, the MEM is utilized to visualize electron density maps from powder diffraction data. Fig. 3h shows the MEM-reconstructed negative electron density maps and sections of negative electron densities in the (100) plane of $K_{1-x}Rb_xAg_4I_5$ (x = 0–0.3) at room temperature. In the (100) plane, the channel formed by alternating Ag1 and Ag2 sites along the [010] crystallographic direction was clearly observed. The distribution of Ag between the Ag1 site indicates a direct hopping between the channels. Overall, MEM reveals a well-defined silver-ion conduction network in $K_{1-x}Rb_xAg_4I_5$, as illustrated in Fig. 4b, which demonstrates the two-dimensional projection of Ag^+ migration pathways along the [010] crystallographic direction. This conduction framework consists of interconnected face-sharing AgI_4 tetrahedral channels primarily aligned along the [010] direction, where the mobile Ag^+ ion preferentially occupies two distinct crystallographic sites, with an optimal inter-site hopping distance of ~1.7 Å between Ag1 and Ag2 positions. Fig. 4a presents the electron density maps projected along the [111] direction, revealing a comprehensive picture of silver-ion migration in $K_{1-x}Rb_xAg_4I_5$. The analysis demonstrates that while the primary conduction pathways for the Ag^+ ion predominantly follow the ⟨010⟩ direction within each plane, the

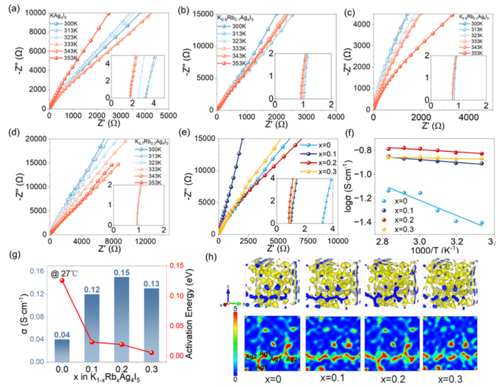

Fig. 3 (a–d) Nyquist plots of $K_{1-x}Rb_xAg_4I_5$ ($x = 0–0.3$) electrolytes at temperatures from 27 °C to 80 °C. The insets are a zoom-in version. (e) Nyquist plots and (f) Arrhenius plots of $K_{1-x}Rb_xAg_4I_5$ ($x = 0–0.3$) electrolytes, where the real-axis impedance is normalized to the respective pellet thickness for better comparison. (g) Comparison of room temperature ionic conductivities and activation energy of $K_{1-x}Rb_xAg_4I_5$ ($x = 0–0.3$) electrolytes. (h) MEM-reconstructed negative electron density maps and sections of negative electron densities in the (100) plane of $K_{1-x}Rb_xAg_4I_5$.

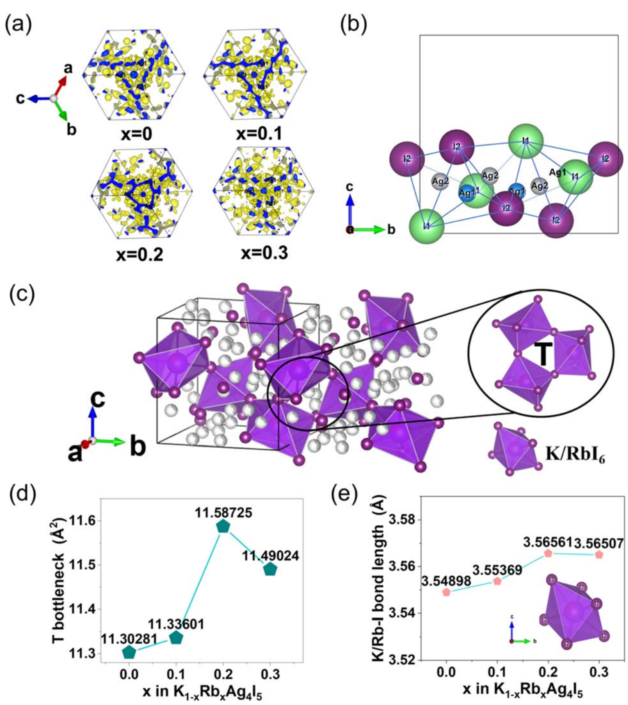

Fig. 4 (a) The electron density map viewed along the [111] direction. (b) The ion conduction pathway model along the [010] direction (the chains of face-sharing anion tetrahedra surrounding the Ag1–Ag2 migration pathway). (c) Crystal structure of $K_{1-x}Rb_xAg_4I_5$ ($x = 0–0.3$) and the typical triangle bottleneck named T-region for the Ag1–Ag2 path. (d) The calculated size of the T-region for $K_{1-x}Rb_xAg_4I_5$ ($x = 0–0.3$). (e) Variation of the Rb–I bond length in the Rb–I octahedra for $K_{1-x}Rb_xAg_4I_5$ ($x = 0–0.3$).

three-dimensional connectivity of the migration network is established through Ag1 sites located along the edges of the unit cell, thereby enabling efficient isotropic silver-ion transport throughout the entire crystal structure. Consequently, the reconstructed real-space distribution reveals that the dominant Ag^+ diffusion in KAg_4I_5 occurs by the continuous pathways along ⟨010⟩ within each plane and well-defined connections between planes *via* the edge-sharing Ag1 positions, which collectively create a fully percolating three-dimensional network for rapid Ag^+ diffusion.

The systematic electrochemical investigation reveals that all samples exhibit exceptionally high ionic conductivity, which we attribute fundamentally to the unique structural characteristics of the iodide framework. Unlike chloride or fluoride counterparts, the larger ionic radius of iodide anions (I^-) induces significantly enhanced polarizability, resulting in a weaker electrostatic binding interaction with mobile silver ions. Fig. 4c shows the crystal structure of the cubic $K_{1-x}Rb_xAg_4I_5$ SEs, where a critical triangle bottleneck named T is signified that dominates the Ag^+ migration across the Ag1–Ag2 channel. According to the refinement results of $K_{1-x}Rb_xAg_4I_5$ ($x = 0–0.3$), the areas of T are calculated and shown in Fig. 4d. In particular, $K_{0.8}Rb_{0.2}Ag_4I_5$ has the largest T area of 11.58 Å^2, which is 1.03 times higher than the pristine KAg_4I_5, supporting enhanced ionic conductivity. Notably, when the doping concentration of Rb^+ reaches 0.3, although the overall unit cell volume increases, the area of T-region shows a slight decrease, resulting in constriction of the ionic conduction channels. This structural modification leads to the observed phenomenon where an expansion of the unit cell volume is accompanied by the reduction in ionic conductivity. Therefore, only at the moderate doping ratios, the enlarged T-region along with the volume effect by Rb^+ doping can play a dominant role in improving the total ionic conductivity. On the other hand, Fig. 4e reveals the evolution of Rb–I bond length within the distorted octahedral cavities, where the six equivalent Rb–I bonds progressively elongate with increasing doping concentration, reaching a maximum length of 3.56 Å at the doping level of 0.2. This bond elongation directly reduces the Rb^+ confinement on the I^- framework, decreasing anion polarizability through more symmetrical electron density distribution, which effectively reduces the coulombic interaction between Ag^+ and I^- sublattice, thereby significantly lowering the migration energy barrier. Subsequent doping beyond this optimal concentration induces a slight contraction of Rb–I bonds, corresponding to a modest reduction in ionic conductivity, demonstrating the delicate balance between structural distortion and ion transport optimization in this superionic conductor system.

An ideal solid electrolyte should possess both high ionic conductivity and excellent electrical insulation to effectively prevent short-circuiting. To evaluate the electronic conductivity of $K_{1-x}Rb_xAg_4I_5$ ($x = 0–0.3$), DC polarization measurements were carried out, as shown in Fig. 5a. A constant potential polarization of 0.4 V was applied at 27 °C. In this experiment, stainless steel was used as a blocking electrode for silver ions, rather than electrons. During the measurement, the current initially exhibits a decline with time until reaching a steady state, where the steady-state current solely corresponds to electron conduction. The formula for calculating the electronic conductivity is given below:

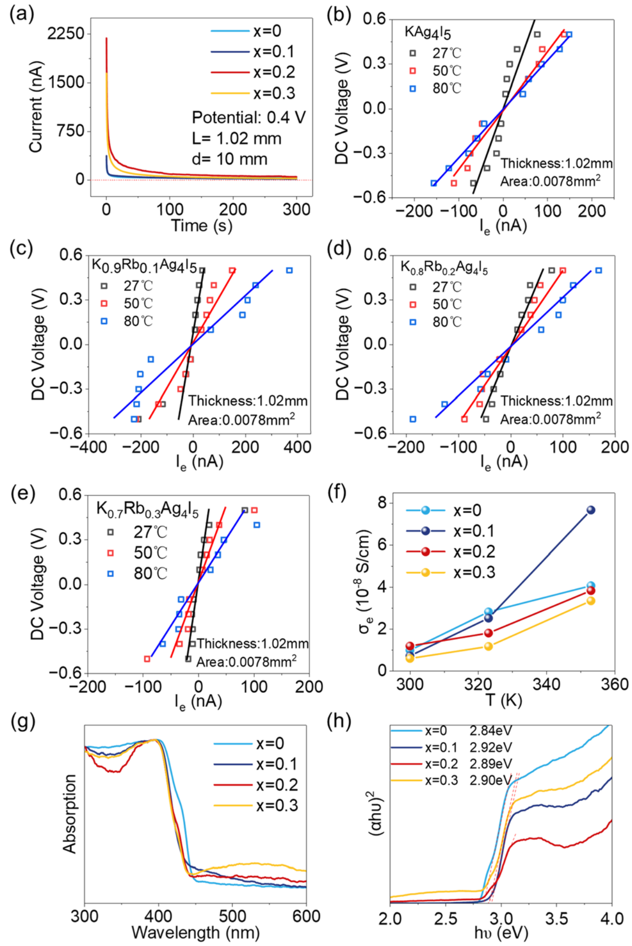

Fig. 5 (a) Direct current (DC) polarization curves of $K_{1-x}Rb_xAg_4I_5$ ($x = 0$–0.3) electrolytes. (b–e) V–I_e curves of $K_{1-x}Rb_xAg_4I_5$ ($x = 0$–0.3) electrolytes, respectively. (f) Temperature-dependent electronic conductivity. (g) Ultraviolet absorption spectrum of $K_{1-x}Rb_xAg_4I_5$ ($x = 0$–0.3) electrolytes. (h) The optical bandgap of the $K_{1-x}Rb_xAg_4I_5$ ($x = 0$–0.3) powder.

$$\sigma_e = \frac{LI}{\pi U r^2} \quad (2)$$

where σ_e represents the electronic conductivity, I refers to the polarization residual current, U denotes the polarization voltage, L represents the thickness, and r corresponds to the radius of the pellets. The current–time curves obtained under different DC polarizations are shown in Fig. S4–S7 (SI) for $K_{1-x}Rb_xAg_4I_5$ ($x = 0$–0.3), respectively. Fig. 5b–e display the V–I_e curves at three temperature points and the corresponding temperature dependence of σ_e in $K_{1-x}Rb_xAg_4I_5$ ($x = 0$–0.3), respectively. All V–I_e plots show good linearity, validating the method in determining σ_e. It is obvious that σ_e of all samples increases gradually with increasing temperature, as indicated by the significantly enhanced I_e values. KAg_4I_5 shows a low σ_e of $\sim 1 \times 10^{-8}$ S cm^{-1} at 27 °C, which increases rapidly to $\sim 4.02 \times 10^{-8}$ S cm^{-1} at 80 °C. Doped samples show lower σ_e values, decreasing from $\sim 1 \times 10^{-8}$ S cm^{-1} for KAg_4I_5 to $\sim 6.1 \times 10^{-9}$ S cm^{-1} for $K_{0.7}Rb_{0.3}Ag_4I_5$ at 27 °C, as shown in Fig. 5f. In addition, all samples show similar temperature dependences of σ_e, suggesting a common origin of the charge carriers (electrons or holes). While all samples show small variations in σ_e, all pellets can be classified as electronic insulators due to their extremely low electronic conductivity of 10^{-8} S cm^{-1}. This value is 6–7 orders of magnitude lower than their ionic conductivity. Therefore, the Rb^+ doped KAg_4I_5 exhibits superior electronic insulation properties. The ultraviolet-visible (UV-Vis) spectra of $K_{1-x}Rb_xAg_4I_5$ ($x = 0$–0.3) compound are shown in Fig. 5g. Apart from the matrix absorption observed below 400 nm, no significant absorption peaks were detected in the visible region. The calculated optical band gap E_g for KAg_4I_5 is 2.84 eV, as shown Fig. 5h. The Rb-doped samples exhibit a slightly increased band gap compared to the pristine sample. The UV-Vis spectroscopy results indicate that all samples possess large band gaps, showing the characteristic of insulating behavior, which is consistent with the electronic conductivity measurements.

4. Conclusions

This study systematically investigates the effects of Rb^+ doping on structural stability and ionic conductivity of KAg_4I_5, achieving an ionic conductivity of 0.15 S cm^{-1} at room temperature, with an exceptionally low activation energy of 19 meV. Ionic transport pathways are visualized directly by the maximum entropy method, revealing that Ag^+ diffusion is predominantly facilitated by ion hopping between the Ag1 and Ag2 sites along the (100) plane. Rb^+ incorporation modifies the local chemical environment in the material, increases the energy barrier for phase transition, thus improving the structural stability of the material. This work not only shows an effective strategy to enhance the performance of KAg_4I_5 solid electrolyte but also provides an efficient and straightforward method to study the diffusion pathways in a given electrolyte.

Conflicts of interest

The authors declare that they have no known competing financial interests or personal relationships that could have appeared to influence the work reported in this paper.

Data availability

The authors confirm that the data supporting the findings of this study are available within the article and its SI.

Supplementary information: supplementary figures (SEM/EDS mappings, TG, DSC, and DC polarization curves), as well as detailed crystallographic refinement tables. See DOI: **https://doi.org/10.1039/d5ta03873a**.

Acknowledgements

This work was supported by the National Natural Science Foundation of China (Grant No. T2125008, 52371234, 92263108, 52302193, 52102277, and 52472238) and the Fundamental Research Funds for the Central Universities, Tongji University.

References

1 B. Reuter and K. Hardel, On the high-temperature modification of silver sulfide iodide, *Nat. Sci.*, 1961, **48**, 161.
2 A. Yoshiasa, F. Kanamaru and K. Koto, Local structure of the superionic conducting α-AgI type $AgI_{1-x}Br_x$ solid-solution, *Solid State Ionics*, 1988, **27**, 275–283.
3 D. Y. Lee and T. Y. Tseng, Unipolar Resistive Switching Characteristics of a ZrO_2 Memory Device with Oxygen Ion Conductor Buffer Layer, *IEEE Electron Device Lett.*, 2012, **33**, 803–805.
4 I. C. Cosentino and R. Muccillo, Properties of thoria-yttria solid electrolytes prepared by the citrate technique, *Mater. Lett.*, 1997, **32**, 295–300.
5 E. Yi, E. Temeche and R. M. Laine, Superionically conducting β″-Al_2O_3 thin films processed using flame synthesized nanopowders, *J. Mater. Chem. A*, 2018, **6**, 12411–12419.
6 D. Lu, Y. Shao, T. Lozano, W. D. Bennett, G. L. Graff, B. Polzin, *et al.*, Failure Mechanism for Fast-Charged Lithium Metal Batteries with Liquid Electrolytes, *Adv. Energy Mater.*, 2015, **5**, 1400993.
7 J. B. Goodenough and K.-S. Park, The Li-Ion Rechargeable Battery: A Perspective, *J. Am. Chem. Soc.*, 2013, **135**, 1167–1176.
8 E. Quartarone and P. Mustarelli, Electrolytes for solid-state lithium rechargeable batteries: recent advances and perspectives, *Chem. Soc. Rev.*, 2011, **40**, 2525–2540.
9 D. H. Kim, D. Y. Oh, K. H. Park, Y. E. Choi, Y. J. Nam, H. A. Lee, *et al.*, Infiltration of Solution-Processable Solid Electrolytes into Conventional Li-Ion-Battery Electrodes for All-Solid-State Li-Ion Batteries, *Nano Lett.*, 2017, **17**, 3013–3020.
10 S. J. Yoo, J. W. Lim and Y.-E. Sung, Improved electrochromic devices with an inorganic solid electrolyte protective layer, *Sol. Energy Mater. Sol. Cells*, 2006, **90**, 477–484.
11 J. Q. Huang, L. P. Shi, E. G. Yeo, K. J. Yi and R. Zhao, Electrochemical Metallization Resistive Memory Devices Using ZnS-SiO_2 as a Solid Electrolyte, *IEEE Electron Device Lett.*, 2012, **33**, 98–100.
12 N. Miura, M. Nakatou and S. Zhuiykov, Impedancemetric gas sensor based on zirconia solid electrolyte and oxide sensing electrode for detecting total NO_x at high temperature, *Sens. Actuators, B*, 2003, **93**, 221–228.
13 H. Yang and N. Wu, Ionic conductivity and ion transport mechanisms of solid-state lithium-ion battery electrolytes: a review, *Energy Sci. Eng.*, 2022, **10**, 1643–1671.
14 J. Minkiewicz, G. M. Jones, S. Ghanizadeh, S. Bostanchi, T. J. Wasely, S. A. Yamini, *et al.*, Large-scale manufacturing of solid-state electrolytes: challenges, progress, and prospects, *Open Ceram.*, 2023, **16**, 100497.
15 Y. Fu, Z. Gu, Q. Gan and Y.-W. Mai, A review on the ionic conductivity and mechanical properties of composite polymer electrolytes (CPEs) for lithium batteries: insights from the perspective of polymer/filler composites, *Mater. Sci. Eng., R*, 2024, **160**, 100815.
16 K. Funke, AgI-type solid electrolytes, *Prog. Solid State Chem.*, 1976, **11**, 345–402.
17 M. Tatsumisago, Y. Shinkuma and T. Minami, Stabilization of superionic α-Agl at room temperature in a glass matrix, *Nature*, 1991, **354**, 217–218.
18 P. Boolchand and W. J. Bresser, Mobile silver ions and glass formation in solid electrolytes, *Nature*, 2001, **410**, 1070–1073.
19 K. Sau, S. Takagi, T. Ikeshoji, K. Kisu, R. Sato, E. C. dos Santos, *et al.*, Unlocking the secrets of ideal fast ion conductors for all-solid-state batteries, *Commun. Mater.*, 2024, **5**, 122.
20 F. Makhlooghiazad, L. A. O'Dell, L. Porcarelli, C. Forsyth, N. Quazi, M. Asadi, *et al.*, Zwitterionic materials with disorder and plasticity and their application as non-volatile solid or liquid electrolytes, *Nat. Mater.*, 2022, **21**, 228–236.
21 J. Ding, M. K. Gupta, C. Rosenbach, H.-M. Lin, N. C. Osti, D. L. Abernathy, *et al.*, Liquid-like dynamics in a solid-state lithium electrolyte, *Nat. Phys.*, 2025, **21**, 118–125.
22 P. Vashishta and A. Rahman, Ionic Motion in α-AgI, *Phys. Rev. Lett.*, 1978, **40**, 1337–1340.
23 V. M. Nield, D. A. Keen, W. Hayes and R. L. McGreevy, Structure and fast-ion conduction in α-AgI, *Solid State Ionics*, 1993, **66**, 247–258.
24 S. Xia, X. Wu, Z. Zhang, Y. Cui and W. Liu, Practical Challenges and Future Perspectives of All-Solid-State Lithium-Metal Batteries, *Chem*, 2019, **5**, 753–785.
25 J. C. Díaz, D. Kitto and J. Kamcev, Accurately measuring the ionic conductivity of membranes via the direct contact method, *J. Membr. Sci.*, 2023, **669**, 121304.
26 J. C. Dyre, P. Maass, B. Roling and D. L. Sidebottom, Fundamental questions relating to ion conduction in disordered solids, *Rep. Prog. Phys.*, 2009, **72**, 046501.
27 A. Chandra, Ion conduction in crystalline superionic solids and its applications, *Eur. Phys. J. Appl. Phys.*, 2014, **66**, 30905.
28 A. Taniguchi, M. Tatsumisago and T. Minami, Crystallization Kinetics of α-Agl in Ag I-Based Silver Orthoborate Glasses, *J. Am. Ceram. Soc.*, 1995, **78**, 460–464.
29 M. Mroczkowska, T. Czeppe, J. L. Nowinski, J. E. Garbarczyk and M. Wasiucionek, DSC and XRD studies on crystallization kinetics in AgI-rich glassy and glass-crystalline ionic conductors of the AgI–Ag_2O–P_2O_5 system, *Solid State Ionics*, 2008, **179**, 202–205.
30 R. Makiura, T. Yonemura, T. Yamada, M. Yamauchi, R. Ikeda, H. Kitagawa, *et al.*, Size-controlled stabilization of the superionic phase to room temperature in polymer-coated AgI nanoparticles, *Nat. Mater.*, 2009, **8**, 476–480.
31 S. Hull, D. A. Keen, D. S. Sivia and P. Berastegui, Crystal Structures and Ionic Conductivities of Ternary Derivatives of the Silver and Copper Monohalides: I. Superionic Phases of Stoichiometry MA_4I_5:$RbAg_4I_5$, KAg_4I_5, and KCu_4I_5, *J. Solid State Chem.*, 2002, **165**, 363–371.
32 B. H. Toby and R. B. Von Dreele, GSAS-II: the genesis of a modern open-source all purpose crystallography software package, *J. Appl. Crystallogr.*, 2013, **46**, 544–549.
33 S. Hull and P. Berastegui, Crystal structures and ionic conductivities of ternary derivatives of the silver and copper monohalides—II: ordered phases within the $(AgX)_x$-

$(MX)_{1-x}$ and $(CuX)_x$-$(MX)_{1-x}$ (M=K, Rb and Cs; X=Cl, Br and I) systems, *J. Solid State Chem.*, 2004, **177**, 3156–3173.

34 M. Sakata and M. Sato, Accurate structure analysis by the maximum-entropy method, *Acta Crystallogr., Sect. A*, 1990, **46**, 263–270.

35 K. Momma, T. Ikeda, A. A. Belik and F. Izumi, Dysnomia, a computer program for maximum-entropy method (MEM) analysis and its performance in the MEM-based pattern fitting, *Powder Diffr.*, 2013, **28**, 184–193.

36 K. Momma and F. Izumi, VESTA 3 for three-dimensional visualization of crystal, volumetric and morphology data, *J. Appl. Crystallogr.*, 2011, **44**, 1272–1276.